Influences of structural anisotropy and heterogeneity on three-dimensional strain fields and cracking patterns of a clay-rich rock

Hailing Shi, Jérôme Hosdez, Thomas Rougelot, S. Xie, J. Shao, J. Talandier

Influences of structural anisotropy and heterogeneity on three-dimensional strain fields and cracking patterns of a clay-rich rock

H.L. Shi[a], J. Hosdez[a], T. Rougelot[a], S.Y. Xie[a], J.F. Shao[a,*], J. Talandier[b]

[a] *Univ. Lille, CNRS, Centrale Lille, UMR9013 - LaMcube - Laboratoire de Mécanique Multiphysique et Multiéchelle, F-59000, Lille, France*
[b] *Andra, 92298 Chatenay Malabry, France*

Abstract

In this study, three-dimensional non-uniform strain fields and cracking patterns of a clay-rich rock are investigated. Uniaxial compression creep tests are performed on samples drilled in five different orientations with respect to bedding planes. A digital volume correlation method is applied to X-ray micro-tomographic images taken during the creep tests to calculate both full local strain fields and average global strains. Both instantaneous and time-dependent strains respectively induced by applied stress and creep mechanism are analysed. Strain heterogeneity inside samples is quantified by calculating strain concentration zones, which are correlated with the presence of stiff inclusions. Cracking patterns of samples are characterised through reconstructed X-ray micro-tomographic images. Correlations between major cracking patterns and strain concentration zones are investigated.

Keywords: Three-dimensional strain field, Cracking pattern, Structural anisotropy, Heterogeneity, Clay-rich rocks, X-ray micro-tomography

*Corresponding author: jian-fu.shao@polytech-lille.fr

Submitted *January 17, 2021*

1. Introduction

Clay-rich rocks are widely encountered in many engineering practices, from classical civil constructions to geological disposal of radioactive waste (Armand et al., 2014, 2017). This class of materials general has multi-scale micro-structures and contains different types of heterogeneities such as stiff and soft inclusions and pores (Ulm and Abousleiman, 2006, Robinet et al., 2012, Bennett et al., 2015, King et al., 2015, Abedi et al., 2016). They are therefore typical heterogeneous materials. Without intending to give an exhaustive review, a number of previous studies have been so far reported on different types of compacted clays and clay-rich rocks, including mechanical properties (Zhang et al., 2012, Yang et al., 2013, Liu et al., 2015a, Togashi et al., 2017, Zhang et al., 2019), swelling properties (Wang et al., 2017, Zeng et al., 2019, Middelhoff et al., 2020), hydric and poromechanical properties (Cariou et al., 2012, Orucoglu et al., 2018).

The emphasis of this study is put on mechanical behaviours of hard clay-rich rocks, in particular instantaneous and creep deformations and failure modes. Among other specificities, the mechanical behaviours of most clay-rich rocks are intimately affected by mineralogical compositions and materials heterogeneities (Hu et al., 2014, Liu et al., 2018a), water content (Hu et al., 2014, Yang et al., 2013, Liu et al., 2018a) and temperature variation (Chen et al., 2014, Menaceur et al., 2015, Liu et al., 2019). Due to the presence of different types of heterogeneities, local strain fields are clearly non-uniform at the samples scales (mm to cm) (Bornert, 2010, Wang et al., 2015). At the same time, cracking is also an important process. On the other hand, most clay-rich rocks exhibit a significant time-dependent creep deformation (Liu et al., 2015a). The creep deformation can be coupled with the time-dependent failure modes generating variation of permeability (Liu

et al., 2015b, 2016). In most clay-rich rocks, the creep deformation mainly occurs inside clay constituents. As another important character, most clay-rich rocks generally exhibit a clear structural anisotropy with the presence of orientated bedding planes (Amadei, 1996, Niandou et al., 1997, Zhang et al., 2012, Yang et al., 2013, Liu et al., 2015a, Togashi et al., 2017, Zhang et al., 2019).

In standard laboratory tests, strain gages and displacement transducers are used to measure global or local (surface) deformation of samples. Further, when long-term creep tests are performed, the reliability of such measuring methods becomes questionable. It is also delicate to use those conventional methods for strongly anisotropic samples. In this study, based on high resolution of X-ray micro-tomographic images, a Digital Volume Correlation (DVC) is adopted to the characterization of both full three-dimensional (3D) strain fields and average macroscopic strains during creep tests of a hard clay-rich rock.

During the last decades, 3D X-ray micro-tomography has become one of the most widely used imaging techniques. This technique has also been successfully applied to rock-like materials, either for the post-mortem analysis of tested samples (Chu et al., 1985, Kawakata et al., 1999, Otani et al., 2000, Bornert, 2010, Chen et al., 2014, Yang et al., 2016) and for the real time monitoring of *in situ* tests. Different kinds of experimental devices have been designed for the real time micro-tomographic monitoring (Viggiani et al., 2013, Pardoen et al., 2020). In some recent studies, multi-modal X-ray and neutron tomography techniques were combined to investigate the water absorption in hard clayey rocks (Stavropoulou et al., 2020). However, *in situ* creep tests with X-ray micro-tomography monitoring have so far been rarely performed on rocks.

On the other hand, different types of mathematical morphology methods have been developed for the treatment of digital images obtained from X-ray tomography. Among them, Digital Image

Correlation (DIC) and DVC are now the popular methods respectively for two-dimensional (2D) and 3D images. Based on high resolution X-ray tomographic images, DVC or DIC based methods has been applied to the characterization of displacement and strain fields in different kinds of materials (Besnard et al., 2006, Stock, 2008, Bornert, 2010, Desbois et al., 2017). In particular, these methods allowed the identification of strain localization and failure modes (Viggiani et al., 2004, Bauer et al., 2006, Desrues et al., 2010, Lenoir et al., 2007, Mao et al., 2019).

The main objective of this study is to investigate the influences of structural anisotropy and materials heterogeneities on the short and long term deformation behaviour and failure modes of a hard clayey rock. For this purpose, uniaxial creep tests are performed on samples drilled in different orientations with respect to bedding planes. 3D X-ray micro-tomographic images are taken during the creep tests. These images are treated by using a DVC based method. Both full strain fields and average macroscopic strains are calculated. Induced cracks patterns leading to sample failure are also identified. The influences of structural anisotropy and materials heterogeneities on deformation behaviour and cracks patterns are analysed through the comparisons between the samples with different loading orientations.

2. Material and samples preparation

In this study, the selected clay-rich rock is the Callovo-Oxfordian (called COx) claystone, which is investigated in the context of geological disposal of radioactive waste in France (Armand et al., 2014, 2017). According to previous micro-structural and mineralogical studies (Robinet, 2008, Robinet et al., 2012, Lenoir et al., 2007), this rock has complex and multi-scale micro-structures. In view of the characterization of mechanical behaviour, the so-called mesoscopic scale

(approximately from 0.1 μm to 100 μm) appears a relevant one. At this scale, the COx claystone is mainly composed of a clay matrix (illite, montmorillonite, kaolinite and a small amount of chlorite), quartz and carbonate grains. The volume fraction of clay matrix is about 40-45%, that of carbonate (mainly calcite) is about 25-35% and that of quartz is about 30%. Other minor minerals, namely feldspar, mica and pyrite, can also be found. The size of quartz and calcite grains is generally less than 100 μm. The majority of pores are found embedded inside the clay matrix at a smaller scale. The emphasis here is put on the mesoscopic scale. The COx claystone is obviously a heterogeneous material at this scale. Under the range of stresses concerned by the geological disposal project (tens of MPa), the quartz and carbonate grains exhibit a linear elastic behaviour. Inelastic deformation and cracking process mainly occur inside the clay matrix (Bésuelle et al., 2006, Lenoir et al., 2007, Bornert et al., 2010, Wang et al., 2015). On the other hand, due to tectonic sedimentation process, like most sedimentary rocks, the COx claystone is also an anisotropic material. As a first approximation, a transversely isotropic representation can be adopted with quasi-horizontal bedding (or stratification) planes (Armand et al., 2014, 2017).

The main objective here is the characterization of non-uniform strain fields in the claystone due to stress variation and creep deformation at the mesoscopic scale. Based on the resolution of X-ray micro-tomography (presented below) and the size of main heterogeneities (quartz and calcite), cylinder samples of small size (~5 mm in diameter and ~10 mm in height) are chosen. The samples are drilled from big cores (about 79 mm in diameter and 300 mm in length), taken at the Bure underground research laboratory (URL) of Andra (French National Agency for radioactive waste management) around the depth of 500 m below the ground surface (Conil et al., 2018). During all the operations, plastic films are used to prevent the loss of moisture in samples. In spite

of all those precautions, the moisture content of some samples was reduced from ~7% to around 4% (Shi et al., 2020b). In order to investigate the influences of structural anisotropy, samples were drilled along five different orientations with respect to bedding planes. The drilling orientation is defined by the angle θ between the drilling axis and bedding planes. The five selected values of θ are $\theta = 0°, 30°, 45°, 60°$ and $90°$ respectively.

3. Experimental methodology

3.1. Procedure of creep tests

Uniaxial compression creep tests are performed. An especial experimental device was designed, allowing applying and maintaining axial stress and taking X-ray micro-tomographic images during creep tests. The experimental device is composed of a manual loading frame, a long transparent cell, a fixed base, a pressure sensor and a data logger, as shown in Figure 1(a). The long transparent cell is made of polycarbonate with good X-ray transmissibility and mechanical stability. The reason for such a long cell is to make the sample and the X-ray source as close as possible, so as to obtain a higher resolution. The force sensor has a range of 100 kg and an accuracy of about 0.01 kg. For the size of samples tested in this study, a maximum axial stress of about 80 kg can be applied. A pair of transparent polycarbonate pistons, as shown in the Figure 1(b), are placed at both ends of the sample, in order to reduce the friction on end surfaces of sample and to obtain clear boundaries in X-ray scanning. The details of experimental device can be found in (Shi et al., 2020a).

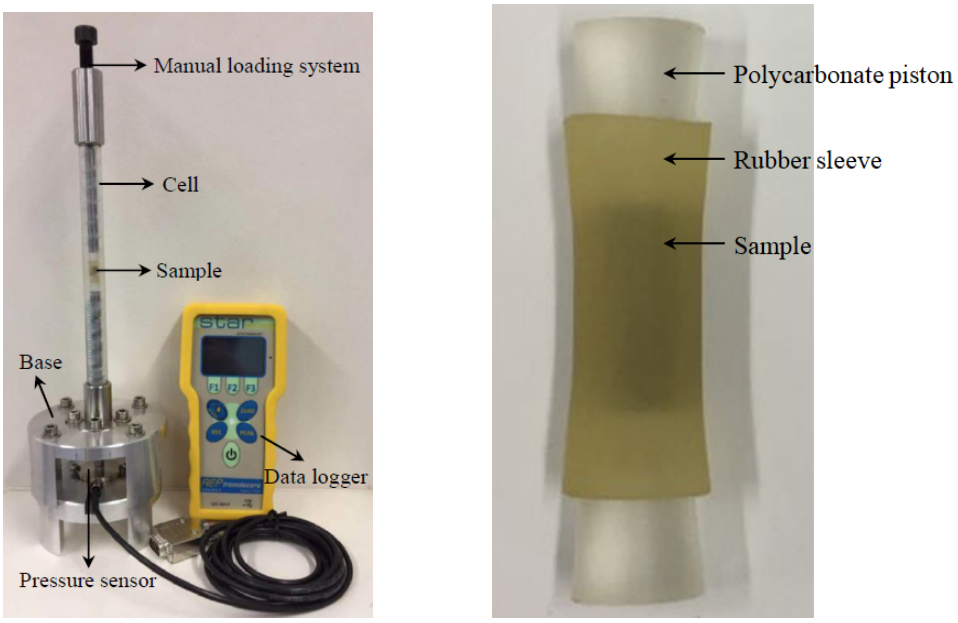

(a) *In situ* creep test system (Shi et al., 2020a,b)

(b) Sample with rubber sleeve and polycarbonate pistons

Figure 1: Physical image of the experimental device for creep tests

Five identical experimental devices are fabricated to perform creep tests on samples drilled in different orientations. Before starting tests, the 3D grey-scale image of each sample is obtained by X-ray micro-tomography in order to detect initial cracks or defeats. Axial stress is increased with 3 to 4 steps. For each loading step, 3D X-ray micro-tomographic images are taken at 3 to 5 different time instances, in order to determine variations of strains induced by applied stress and creep process. However, in order to conveniently choose axial stress values for different loading steps, preliminary uniaxial compression tests are first realized to get an estimation of peak stress. The obtained values of uniaxial compression strength, elastic properties of the five selected samples as well as loading steps for creep tests are presented in Table 1. It is worth noticing that the values of uniaxial compression strength obtained here are higher than the average values reported in previous works (Liu et al., 2018a,b, Zhang et al., 2019). The difference is probably due to the

fact that the water content of the small size samples used here is lower than that of the large size samples used in most previous studies.

Table 1: Elastic and strength properties of five samples with different orientations and stress steps for creep tests

Rock Core	Orientation	Diameter (mm)	Height (mm)	Peak stress q_{peak}/(MPa)	Creep stress steps q_c/q_{peak}/(%)	Axial elastic modulus E/(GPa)	Poisson's Ratio ν
EST58125	0°	4.87	10.65	35.0	41, 60, 77, 94	~ 10.0	0.18 – 0.20
EST58125	30°	4.85	10.88	21.8	56, 77, 100	~ 8.5	0.20 – 0.26
EST58125	45°	4.84	10.88	27.7	40, 67, 90	~ 8.0	0.15 – 0.24
EST58125	60°	4.85	10.92	29.3	40, 57, 82, 100	~ 7.5	0.22 – 0.26
EST58125	90°	4.96	9.54	36.0	40, 60, 70, 90	~ 6.3	0.26 – 0.30

3.2. Strain characterization method

3D strain fields are calculated by using DVC method applied to X-ray micro-tomographic images of samples taken during creep tests. A detailed description of DVC method can be found in (Bay et al., 1999, Shi et al., 2020b). A recent review on DVC method can be found in (Buljac et al., 2018). The basic principle of DVC is to determine the 3D displacement vector of each individual volume element by comparing two 3D digital images before and after deformation of the same element. Each image is identified by its grey scale function. It is assumed that the grey scale variations are only due to the displacement of material points.

In this study, the DVC calculation is carried out with the YaDICs software (Seghir et al., 2014). A window size of 8×8×8 pixels is chosen to ensure a good spatial resolution thanks to the good natural speckle pattern of the COx claystone in X-ray micro-tomography.

3D images of tested samples are taken by using the In Situ Innovative Set-ups under X-ray Micro-tomography platform (ISIS4D) (Limodin et al., 2013). Detailed descriptions of micro-

tomographic imaging technique can be found in (Kak and Slaney, 2001, Goldman, 2007). In this study, the operation voltage is set at 100 kV and the filament current is set to 45 μA in order to achieve a spatial resolution of $4.5 \times 4.5 \times 4.5$ μm^3/pixel. This resolution is required to capture the microstructure evolution of the COx claystone during creep tests. Reconstruction of the tomographic data is performed with a filtered back projection algorithm using X-act software (Shi et al., 2020b).

4. Main results and discussions

4.1. Analysis of average strains and stresses

Based on the strains of all elements calculated by using the DVC method, the average (or global) strains of the tested samples are determined. In the context of uniaxial compression creep tests, the axial and radial strains are considered. In Figure 2, one shows the evolutions of accumulated axial and radial strains with time for five samples drilled along different orientations ($\theta = 0°, 30°, 45°, 60°$ and $90°$). The sudden increases of strains in this Figure correspond to the variations induced by the raise of axial stress. The variations with time between two successive loading steps are related to creep strains under constant axial stress. One can observe obvious differences between five samples. That clearly indicates that the COx claystone exhibits an anisotropic deformation behaviour. More precisely, for the axial strain, the maximum value is obtained for the sample with $\theta = 90°$ while minimum is for $\theta = 0°$. For the radial strain, it seems that the maximum strain is observed on the sample with $\theta = 45°$. These results are consistent with the anisotropic micro-structure of material. Indeed, for the sample with $\theta = 90°$, the axial stress is perpendicular to bedding planes. Thus, the bedding planes are compacted by the axial

stress, enhancing the compressive axial strain. For the sample with $\theta = 45°$, the bedding planes are subjected to the maximum shear stress and exhibit important sliding. This should enhance the evolution of extensive radial strain.

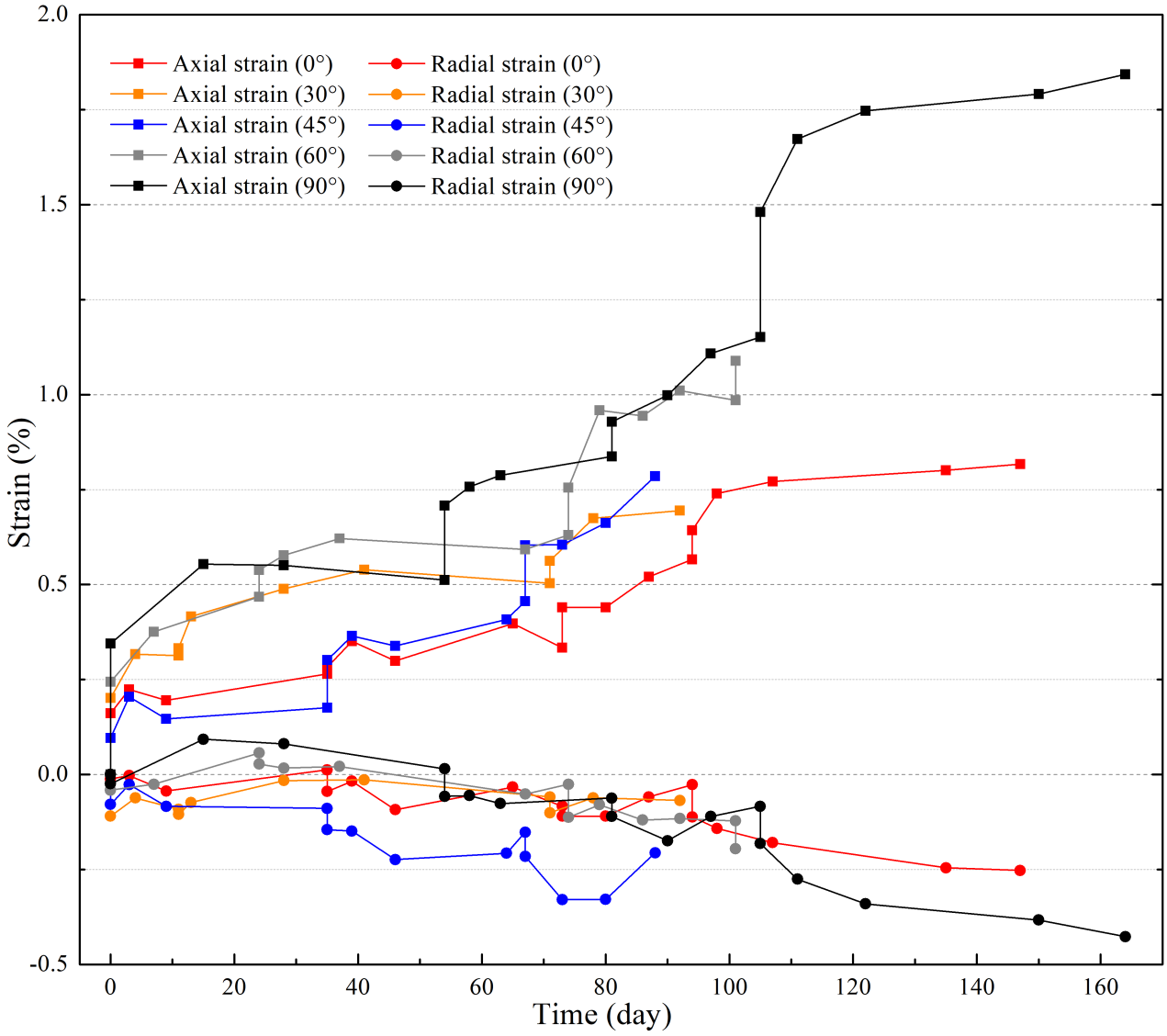

Figure 2: Evolutions of average axial and radial strains with time for five samples with different loading orientations during uniaxial compression creep tests

In order to quantify the strain heterogeneity of samples, the following simple heterogeneity

ratio parameter β_h is introduced here:

$$\beta_h = ({\epsilon_\alpha}^{max} - {\epsilon_\alpha}^{min})/|{\epsilon_\alpha}^{min}| \ , \ \ \alpha = axial, radial \tag{1}$$

where ${\epsilon_\alpha}^{max}$ and ${\epsilon_\alpha}^{min}$ are the maximum and minimum axial or radial strains of computing elements (each element contains 512 pixels). In Figure 3, the variations of β_h with loading time are given for five samples. It is very clear that the heterogeneity of radial strains is much more significant than that of axial ones. Indeed, the value of β_h varies around 1 for the axial strain while it can be higher than 6 for the radial one. Moreover, the strain heterogeneity is also influenced by loading orientation. The maximum value of β_h is found on the radial strain for the sample with $\theta = 45°$. Finally, the value of β_h shows a significant increase with loading time. This means that the local strain fields of five samples become more and more heterogeneous when the axial stress is increased and creep deformation progresses.

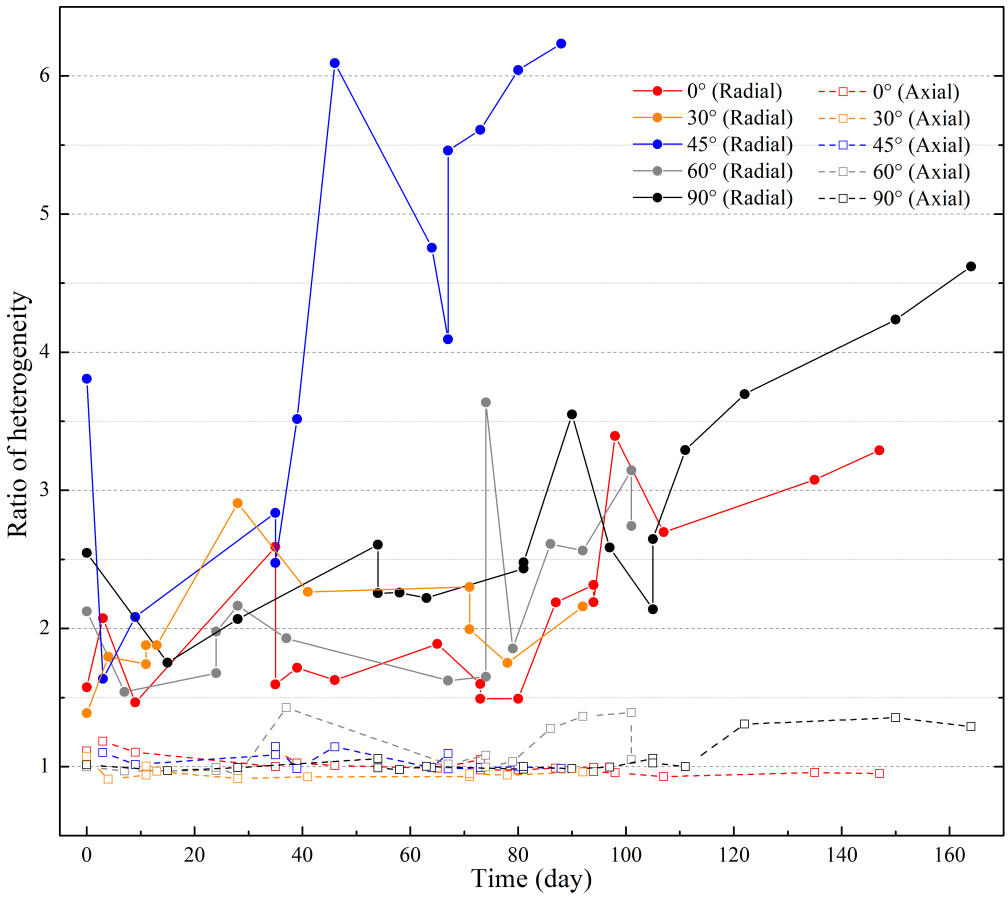

Figure 3: Variations of strain heterogeneity ratio β_h during creep tests for five samples with different loading orientations

In Figure 4, we show the variations of axial and radial strains calculated from the last scan images (the last points of strain curves in Figure 2) as functions of loading orientation. The values represent the strains just before the complete failure of samples. It can be seen that the axial strain exhibits a stronger anisotropy than the radial one. The axial strain is always maximal for the sample with $\theta = 90°$ while it is nearly the same for the samples with $\theta = 0°$, $\theta = 30°$ and $\theta = 40°$. On the same Figure, one can also see that the anisotropy of radial strain is less obvious and more difficult to interpret than the axial one. This may be due to the fact that the heterogeneity of radial strain fields is much stronger than that of the axial strain, as shown in Figure 3.

Further, the values of failure axial stress are also reported in Figure 4, as functions of loading orientation. It is clear that the uniaxial compression strength is strongly dependent on loading orientation. The maximum and minimum failure stresses are obtained respectively on the samples with $\theta = 90°$ and $\theta = 30°$. The failure strength of the sample with $\theta = 0°$ (parallel to bedding planes) is quite close to that of the sample with $\theta = 90°$ (perpendicular to bedding planes). However, the failure stresses of the samples with a loading orientation between $\theta = 30°$ and $\theta = 60°$ are significantly lower than those of two principal directions. This can be explained by the fact that the failure process in these inclined samples is enhanced by the sliding along bedding planes. These results are consist with those reported in previous works on clay-rich rocks (Amadei, 1996, Niandou et al., 1997, Zhang et al., 2012, Yang et al., 2013, Liu et al., 2015a, Togashi et al., 2017, Zhang et al., 2019).

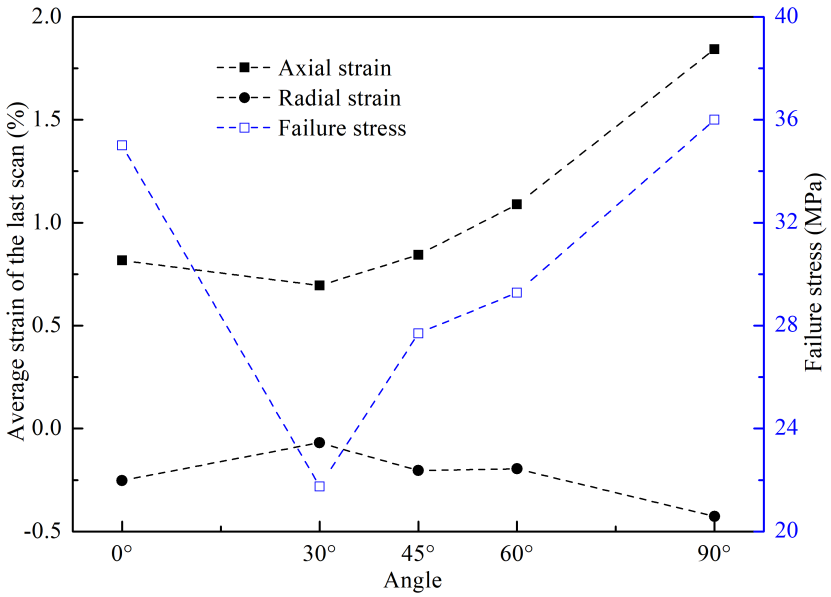

Figure 4: Failure stress of five samples with different loading orientations relative to the bedding planes

4.2. *Analysis of full strain fields*

With the help of DVC method, full 3D strain fields of the tested samples can be determined. As examples, in Figure 5, one presents the distributions of accumulated axial strain of two samples respectively with $\theta = 45°$ and $90°$, at different values of axial stress and creep time. It is interesting to observe that the orientations of the strain concentration bands are clearly correlated to those of bedding planes. It seems that the strain localization is also affected by the structural anisotropy of materials. It should be reminded that Figure 5(a) and 5(d) are the grayscale maps of the initial state of the two samples. It is difficult to directly observe the bedding planes by X-ray micro-tomography.

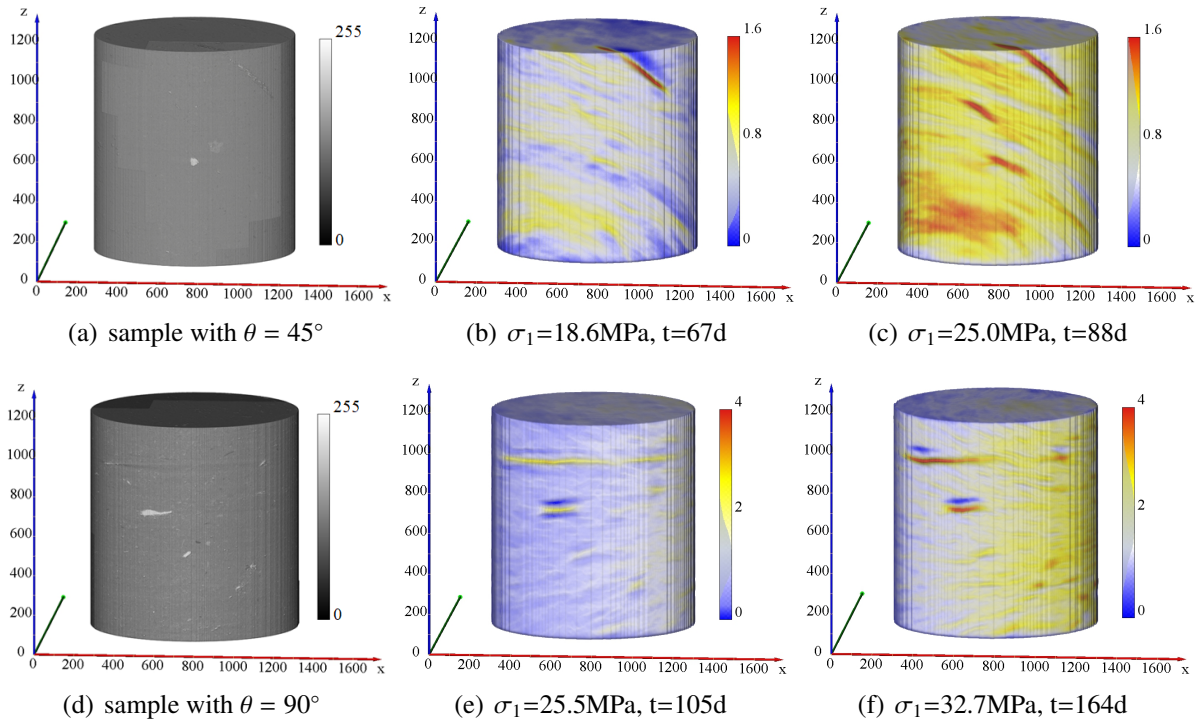

(a) sample with $\theta = 45°$ (b) σ_1=18.6MPa, t=67d (c) σ_1=25.0MPa, t=88d

(d) sample with $\theta = 90°$ (e) σ_1=25.5MPa, t=105d (f) σ_1=32.7MPa, t=164d

Figure 5: Distributions of accumulated axial strain (in %) in the samples with $\theta = 45°$ and $\theta = 90°$ at different axial stress levels and creep time: (a) and (d) are the grayscale maps of the initial state of the two samples; (b) and (c) are the axial strain distributions of the sample with $\theta = 45°$; (e) and (f) are the axial strain distributions of the sample with $\theta = 90°$

In order to get a detailed analysis of strain localization process, strain concentration zones (SCZ) are here defined including all calculated elements whose strains are higher than twice the average strain of sample. Two examples of SCZs are presented in Figure 6 for the samples with $\theta = 45°$ and $\theta = 90°$ at a selected axial stress value and creep time.

For the sample with $\theta = 45°$, the locations of axial SCZs basically coincide with those of the radial ones. The extents of SCZs expand with axial stress level and creep time (not shown in this Figure). One can also find that the SCZs are correlated with high-density zones of the sample. These high-density zones are mainly metal oxide accumulation zones. In the process of geological deposition, metal oxidation is accompanied by a large amount of hydrogen production, which results in a large number of tiny pores (nano- to micro-) in the clay matrix surrounding the metal oxide zones. Therefore, the strain concentrated is enhanced in these weak porous material zones.

For the sample with $\theta = 90°$, there is no obvious correlation between the axial and radial SCZs. The axial SCZs have a correlation with the high-density zones, like the sample with $\theta = 45°$. However, the radial SCZs are quite diffuse and located in the right half part of sample. It seems that the radial strain distribution is clearly dissymmetrical with respect to the sample axis. This can be due to strong material heterogeneity or experimental artefact (for example, the applied stress is not completely parallel to the sample axis).

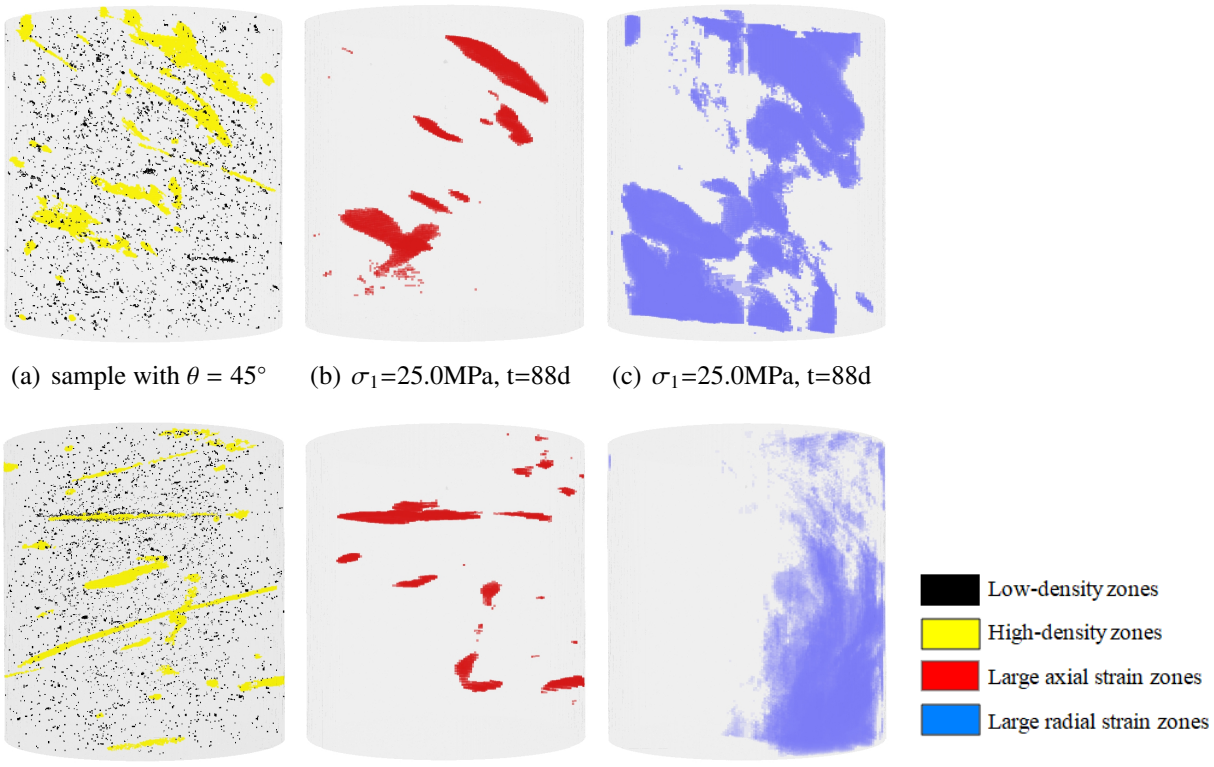

(a) sample with $\theta = 45°$ (b) σ_1=25.0MPa, t=88d (c) σ_1=25.0MPa, t=88d

(d) sample with $\theta = 90°$ (e) σ_1=32.7MPa, t=150d (f) σ_1=32.7MPa, t=150d

Figure 6: Locations of strain concentration zones (higher than twice the average strain) in two samples with $\theta = 45°$ and $\theta = 90°$ at selected axial stress values and creep time: (a) and (d) are the grayscale maps of the initial state of the two samples; (b) and (c) are the distributions of low-density and high-density zones of the sample with $\theta = 45°$; (e) and (f) are the distributions of low-density and high-density zones of the sample with $\theta = 90°$

4.3. Analysis of creep strain fields

After the discussion of accumulated strains, the emphasis is here put on the strain variations due to creep process of the COx claystone. For this purpose, strain increments during a selected constant stress level are analysed. The sample with $\theta = 90°$ is taken as an example. More especially, the creep step under the axial stress of 32.7 MPa is considered. Incremental variations of both axial and radial strains with time are calculated and their 3D distributions are presented in Figure 7 for different time instances. Main zones of large stiff inclusions inside the sample are also

indicated (zones ① ~ ④ marked in Figure 7(a)). It is clear that the creep strain fields are strongly non-uniform at the sample scale. Like the accumulated axial strain, the concentration process of axial creep strain is enhanced by the presence of stiffness inclusions. Compared with the results shown in Figure 5, it seems that the evolutions of local creep strain around stiff inclusions are more prominent than those of instantaneous strain induced by applied stress raise. Concerning the radial creep deformation, both tensile and compressive strain zones are found. However, the concentration of radial creep strain is not clearly influenced by the stiff inclusions, similarly to the instantaneous radial strain. In Figure 8, the distributions of incremental axial creep strain on the longitudinal section of sample are presented for two time instances. Again, one can observe the correlation between the axial creep strain concentration and stiff inclusions zones. Further, it is found that the influence of loading orientation on the creep strain variation is less significant than that on the instantaneous strain induced by applied stress (not shown here).

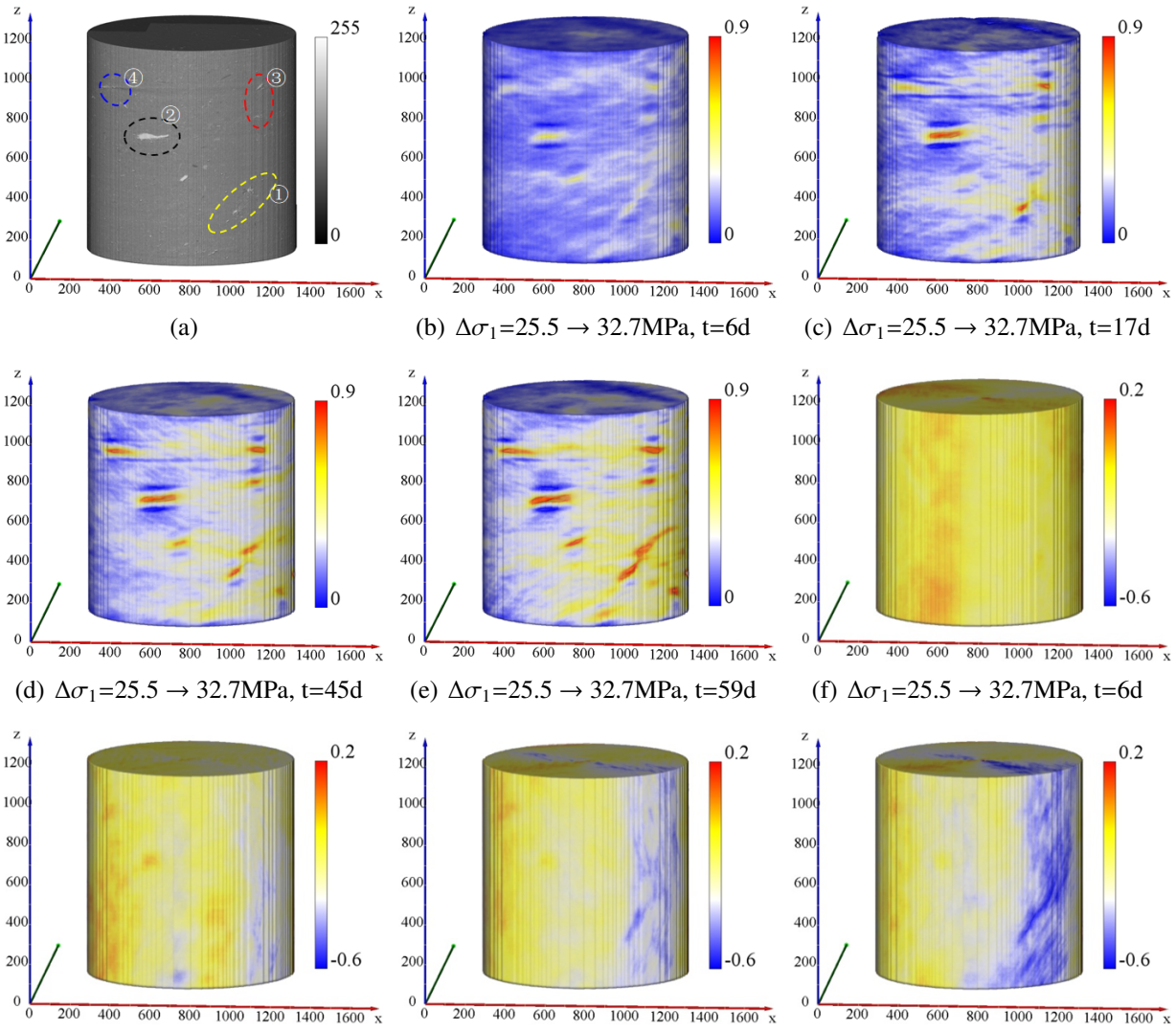

(a) (b) $\Delta\sigma_1$=25.5 → 32.7MPa, t=6d (c) $\Delta\sigma_1$=25.5 → 32.7MPa, t=17d

(d) $\Delta\sigma_1$=25.5 → 32.7MPa, t=45d (e) $\Delta\sigma_1$=25.5 → 32.7MPa, t=59d (f) $\Delta\sigma_1$=25.5 → 32.7MPa, t=6d

(g) $\Delta\sigma_1$=25.5 → 32.7MPa, t=17d (h) $\Delta\sigma_1$=25.5 → 32.7MPa, t=45d (i) $\Delta\sigma_1$=25.5 → 32.7MPa, t=59d

Figure 7: Distributions of incremental axial and radial creep strains (in %) in the sample with $\theta = 90°$ at different time instances and under a constant stress of 32.7 MPa: (a) is the grayscale map of the initial state; (b) to (e) are the distributions of axial strains; (f) to (i) are the distributions of radial strains

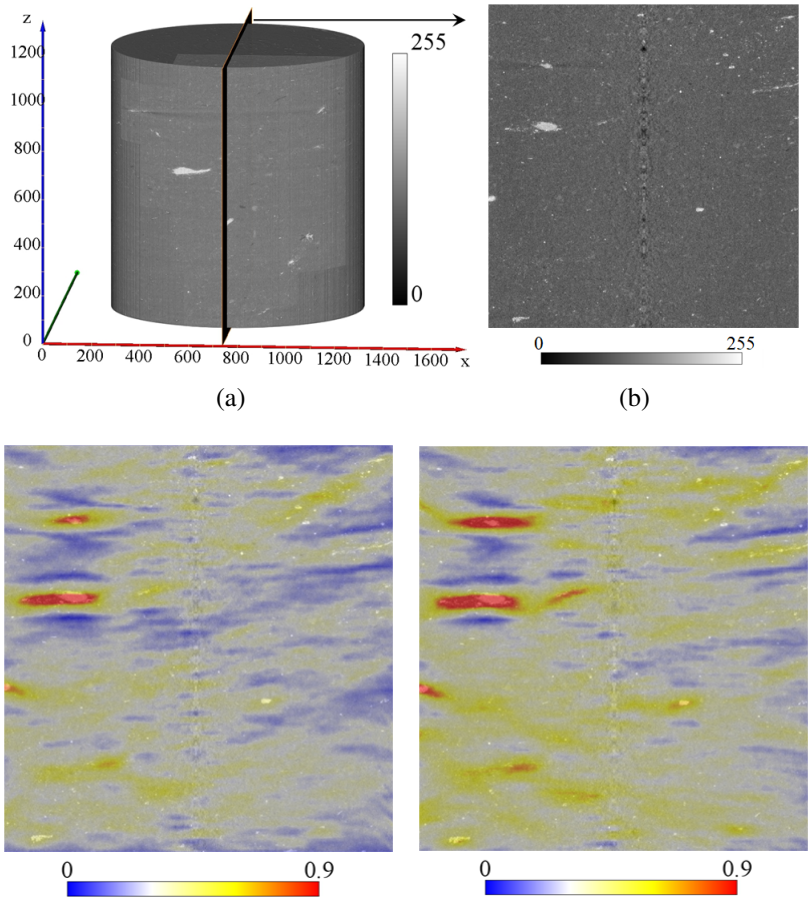

(a) (b)

(c) $\Delta\sigma_1$=25.5 → 32.7MPa, t=45d (d) $\Delta\sigma_1$=25.5 → 32.7MPa, t=59d

Figure 8: Distributions of incremental axial creep strain (in %) on the longitudinal section of sample with $\theta = 90°$ at two time instances and under a constant stress of 32.7 MPa: (a) shows the position of the selected longitudinal section in the sample; (b) is the grayscale map of the selected longitudinal section

4.4. Analysis of failure modes

Thanks to the advanced computed tomography imaging technology, 3D cracks patterns can be reconstructed. In Figure 9, one shows the distributions of cracks in five samples with different loading orientation just after the final failure. It is seen that the cracking mode of the anisotropic COx claystone is clearly influenced by the loading orientation with respect to bedding planes. For the samples with small orientation angles, namely $\theta = 0°$ and $\theta = 30°$, multiple quasi vertical and

through cracks are observed. These cracks are generally driven by the tensile radial (or lateral) strain and closely correlated with the burst (or opening) of bedding planes. For the sample with $\theta = 45°$, a single major inclined crack is obtained and nearly parallel to bedding planes. This is a closed shear crack mainly driven by the sliding along bedding planes. For the samples with high orientation angles, say $\theta = 60°$ and $\theta = 90°$, complex cracks patterns are observed. Large cracked zones are generated in the samples. Although the cracking process cannot be captured, we infer that there are some competitions between structural bedding planes and induced cracks. Further, the cracked zones are localized near the up or bottom ends of samples. The failure modes in these two samples is probably influenced by the boundary conditions such as the friction between samples and bases. Nevertheless, in Figure 10, we present the superposition of cracking pattern and creep strain distribution at a selected loading step for the sample with $\theta = 90°$. It seems that the occurrence and propagation of major cracks are correlated with the creep strain concentration zones. Although many strain concentration zones (red zones) appear in the axial creep strain distribution, most of the strain concentration zones are quasi-parallel to the bedding planes. Only the strain concentration zone coinciding with the failure crack is inclined to the bedding planes. In addition, the failure crack extends upward from the middle of the sample end. As discussed previously, there may be some competitions between the structural bedding planes and the induced cracks, and the failure crack may be influenced by the boundary conditions. For the radial creep strain, the maximum strain concentration zone coincides well with the position of the failure crack. More studies on cracking pattern and creep strain distribution will be continued in the future.

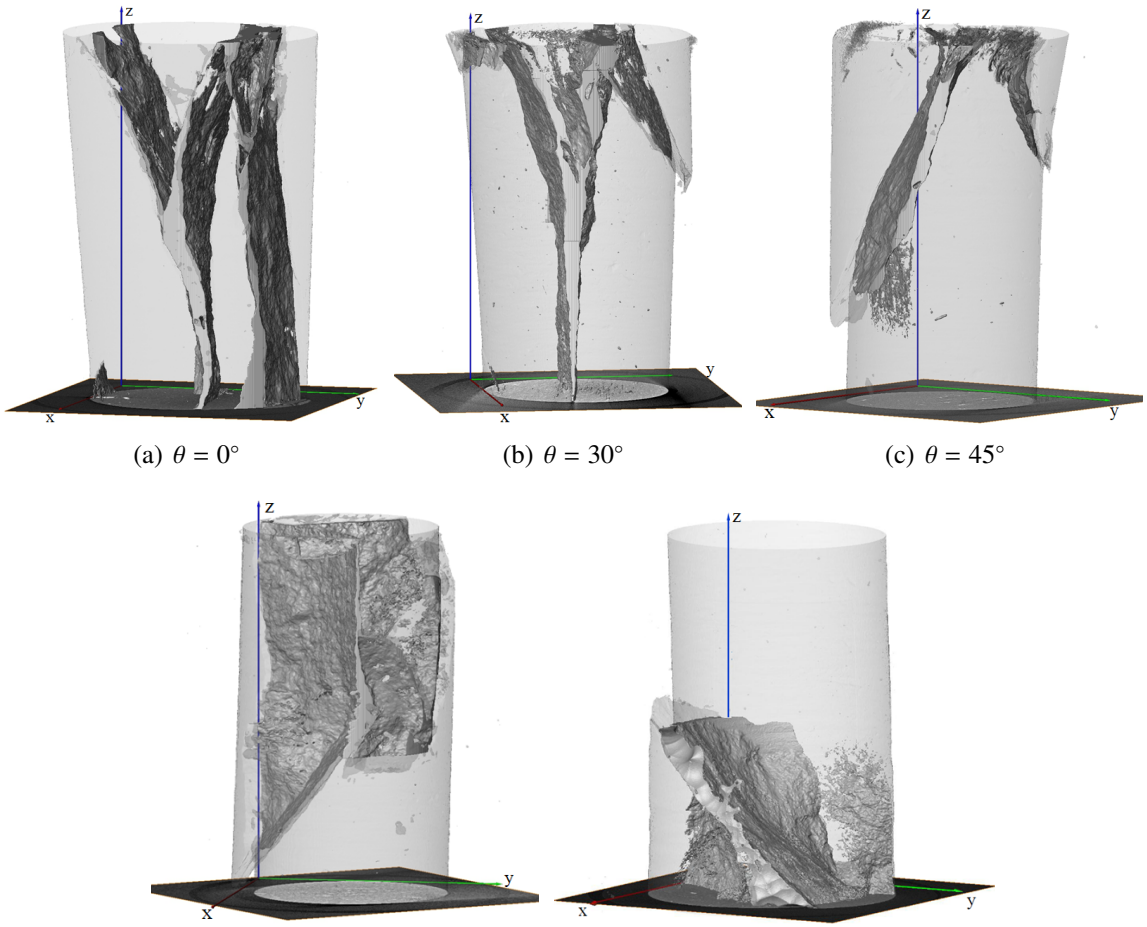

(a) $\theta = 0°$ (b) $\theta = 30°$ (c) $\theta = 45°$

(d) $\theta = 60°$ (e) $\theta = 90°$

Figure 9: 3D reconstructed cracks in five samples with different loading orientations at the last scan time just before failure

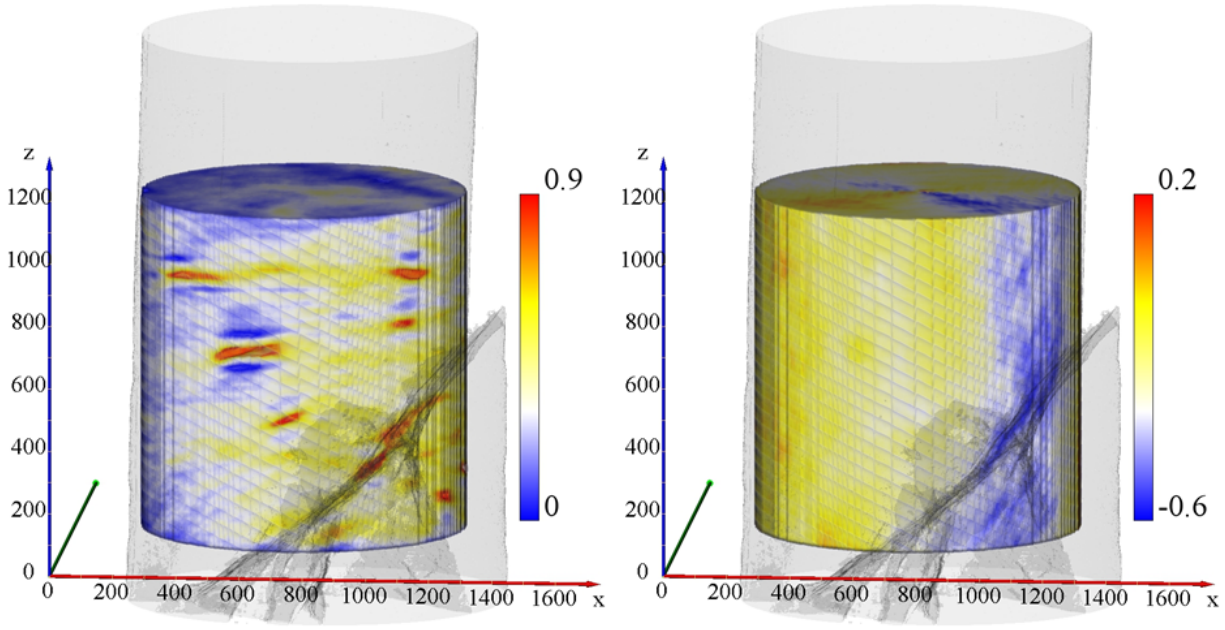

(a) $\Delta\sigma_1$=25.5 → 32.7MPa, t=59d (axial strain) (b) $\Delta\sigma_1$=25.5 → 32.7MPa, t=59d (radial strain)

Figure 10: Correlation between creep strain concentration zones and generation of major cracks in the sample with $\theta = 90°$

5. Conclusions

In this study, the digital volume correlation method was applied to X-ray micro-tomographic images to investigate the deformation behaviour and failure modes of a clay-rich rock, the Callovo-Oxfordian claystone. Both the instantaneous and time-dependent strains respectively induced by stress variation and creep mechanism were investigated. Full 3D strain fields and average macroscopic strains have been calculated. 3D cracks patterns have also been reconstructed. Based on the obtained results, the following main remarks can be drawn.

Due to materials heterogeneities such as stiff inclusions and pores, the strain fields of the COx claystone are clearly non-uniform at the sample scale. Under uniaxial compression condition, the heterogeneity of radial strain is much more important than that of the axial one. Further, the strain

concentration (or localisation) is accentuated with the increase of applied stress. The deformation behaviour of the clay-rich rock is also strongly anisotropic mainly due to the presence of bedding planes. The local strain fields as well as the average macroscopic strains are clearly influenced by loading orientation as the consequences of compaction (or opening) and sliding of bedding planes.

The COx claystone exhibits a significant creep process at the time scale considered here. The local distributions of creep strains are more sensitive to the presence of materials heterogeneities such as stiff inclusions than that of bedding planes.

The failure strength of the COx claystone is also strongly dependent on the loading orientation. The minimum of strength is generally obtained when the maximum shear stress plane is quasi parallel to bedding planes while the maximum one corresponds to the situations where the major compressive stress is either perpendicular or parallel to bedding planes.

The cracking patterns of the COx claystone samples are clearly affected by the structural anisotropy. Cracks of tensile splitting type are generated for small orientation angles (between the major compressive stress and bedding planes). Closed shear cracks are observed when the maximum shear stress plane is quasi parallel to bedding planes. Complex cracked zones are formed the major compressive stress is nearly perpendicular to bedding planes.

Only uniaxial compression tests are performed in the present study. In our ongoing studies, triaxial compression paths are considered in order to investigate effects of confining stress on deformation and failure behaviours of clay-rich rocks.

Acknowledgements

The present study was jointly supported by Andra and the ISIS4D X-Ray CT platform. This platform has been funded by the International Campus on Safety and Inter-modality in Transportation (CISIT), the Hauts-de-France Region, the European Community and the National Center for Scientific Research (CNRS). Special thanks are addressed to Jean-Pierre Parent and Jean Secq for their invaluable assistance to the design of experimental device and preparation of samples.

References

Abedi, S., Slim, M., Hofmann, R., Bryndzia, T., Ulm, F. J., 2016. Nanochemo-mechanical signature of organic-rich shales: a coupled indentation-edx analysis. Acta Geotechnica 11, 559–572.

Amadei, B., 1996. Importance of anisotropy when estimating and measuring in situ stresses in rock. In: International Journal of Rock Mechanics and Mining Sciences & Geomechanics Abstracts. Vol. 33. Elsevier, pp. 293–325.

Armand, G., Conil, N., Talandier, J., Seyedi, D. M., 2017. Fundamental aspects of the hydromechanical behaviour of callovo-oxfordian claystone: from experimental studies to model calibration and validation. Computers and Geotechnics 85, 277–286.

Armand, G., Leveau, F., Nussbaum, C., deLaVaissiere, R., Noiret, A., Jaeggi, D., Landrein, P., Righini, C., 2014. Geometry and properties of the excavation induced fractures at the meuse-haute-marne url drifts. Rock Mech. Rock Eng. 47, 21–41.

Bauer, A., Verhulp, E., Schoofs, S., 2006. Measuring local strains in sandstones under stress with microcomputed tomography. Advances in x-ray tomography for geomaterials, 247–253.

Bay, B. K., Smith, T. S., Fyhrie, D. P., Saad, M., 1999. Digital volume correlation: three-dimensional strain mapping using x-ray tomography. Experimental mechanics 39 (3), 217–226.

Bennett, K. C., Berla, L. A., Nix, W. D., Borja, R. I., 2015. Instrumented nanoindentation and 3d mechanistic modeling of a shale at multiple scales. Acta Geotechnica 10, 1–14.

Besnard, G., Hild, F., Roux, S., 2006. Finite element displacement fields analysis from digital images application to portevin le chatelier bands. Experimental Mechanics 46, 789–803.

Bésuelle, P., Viggiani, G., Lenoir, N., Desrues, J., Bornert, M., 2006. X-ray micro ct for studying strain localization in clay rocks under triaxial compression. Vol. 118. John Wiley & Sons, pp. 35–52.

Bornert, M., 2010. X-ray micro ct for studying strain localization in clay rocks under triaxial compression. Advances in X-ray Tomography for Geomaterials 118, 35–52.

Bornert, M., Vales, F., Gharbi, H., Nguyen Minh, D., 2010. Multiscale full-field strain measurements for micromechanical investigations of the hydromechanical behaviour of clayey rocks. Strain 46 (1), 33–46.

Buljac, A., Jailin, C., Mendoza, A., Neggers, J., TaillandierThomas, T., Bouterf, A., Smaniotto, B., Hild, F., Roux, S., 2018. Digital volume correlation review of progress and challenges. Experimental Mechanics 58, 661–708.

Cariou, S., Duan, Z., Davy, C., Skoczylas, F., Dormieux, L., 2012. Poromechanics of partially saturated cox argillite. Applied Clay Science 56, 36–47.

Chen, G., Maes, T., Vandervoort, F., Sillen, X., Van Marcke, P., Honty, M., Dierick, M., Vanderniepen, P., 2014. Thermal impact on damaged boom clay and opalinus clay: permeameter and isostatic tests with μct scanning. Rock mechanics and rock engineering 47 (1), 87–99.

Chu, T., Ranson, W., Sutton, M. A., 1985. Applications of digital-image-correlation techniques to experimental mechanics. Experimental mechanics 25 (3), 232–244.

Conil, N., Talandier, J., Djizanne, H., de La Vaissière, R., Righini-Waz, C., Auvray, C., Morlot, C., Armand, G., 2018. How rock samples can be representative of in situ condition: A case study of callovo-oxfordian claystones. Journal of Rock Mechanics and Geotechnical Engineering 10 (4), 613–623.

Desbois, G., Höhne, N., Urai, J. L., Bésuelle, P., Viggiani, G., 2017. Deformation in cemented mudrock (callovo-oxfordian clay) by microcracking, granular flow and phyllosilicate plasticity: insights from triaxial deformation, broad ion beam polishing and scanning electron microscopy. Solid Earth 8 (2), 291–305.

Desrues, J., Viggiani, G., Besuelle, P., 2010. Advances in X-ray Tomography for Geomaterials. Vol. 118. John Wiley & Sons.

Goldman, L. W., 2007. Principles of ct and ct technology. Journal of nuclear medicine technology 35 (3), 115–128.

336 Hu, D. W., Zhang, F., Shao, J. F., Gatmiri, B., 2014. Influences of mineralogy and water content on the mechanical
337 properties of argillite. Rock mechanics and rock engineering 47, 157–166.
338 Kak, A. C., Slaney, M., 2001. Principles of computerized tomographic imaging. Vol. Classics in applied mathematics,
339 33. Society for Industrial and Applied Mathematics, Philadelphia.
340 Kawakata, H., Cho, A., Kiyama, T., Yanagidani, T., Kusunose, K., Shimada, M., 1999. Three dimensional observa-
341 tions of faulting process in westerly granite under uniaxial and triaxial conditions by x-ray ct scan. Tectonophysics
342 313 (3), 293–305.
343 King, H. E., Eberle, A. P. R., Walters, C. C., Kliewer, C. E., Ertas, D., Huynh, C., 2015. Pore architecture and
344 connectivity in gas shale. Energy Fuels 29, 1375–1390.
345 Lenoir, N., Bornert, M., Desrues, J., Bésuelle, P., Viggiani, G., 2007. Volumetric digital image correlation applied to
346 x-ray microtomography images from triaxial compression tests on argillaceous rock. Strain 43 (3), 193–205.
347 Limodin, N., Rougelot, T., Hosdez, J., 2013. Isis4d - in situ innovative set-ups under x-ray microtomography.
348 http://isis4d.univ-lille.fr.
349 Liu, Z., Shao, J., Liu, T., Xie, S., Conil, N., 2016. Gas permeability evolution mechanism during creep of a low
350 permeable claystone. Applied Clay Science 129, 47–53.
351 Liu, Z., Shao, J., Xie, S., Conil, N., Zha, W., 2018a. Effects of relative humidity and mineral compositions on creep
352 deformation and failure of a claystone under compression. International Journal of Rock Mechanics and Mining
353 Sciences 103, 68–76.
354 Liu, Z., Xie, S., Shao, J., Conil, N., 2015a. Effects of deviatoric stress and structural anisotropy on compressive creep
355 behavior of a clayey rock. Applied Clay Science 114, 491–496.
356 Liu, Z., Xie, S., Shao, J., Conil, N., 2018b. Multi-step triaxial compressive creep behaviour and induced gas perme-
357 ability change of clay-rich rock. Géotechnique 68 (4), 281–289.
358 Liu, Z. B., Shao, J. F., Xie, S. Y., Conil, N., Talandier, J., 2019. Mechanical behavior of claystone in lateral decom-
359 pression test and thermal effect. Rock Mechanics and Rock Engineering 52, 321–334.
360 Liu, Z. B., Shao, J. F., Xie, S. Y., Secq, J., 2015b. Gas permeability evolution of clayey rocks in process of compressive
361 creep test. Materials Letters 139, 422–425.

Mao, L., Zhu, Y., Wang, Y., Liu, Y., Li, L., Chiang, F.-p., 2019. An improved digital volumetric speckle photography technique with x-ray microtomography and its applications to investigating strain localization in red sandstone. Rock Mechanics and Rock Engineering in press, 1–10.

Menaceur, H., Delage, P., Tang, A. M., Conil, N., 2015. The thermo-mechanical behaviour of the callovo-oxfordian claystone. International Journal of Rock Mechanics and Mining Sciences 78, 290–303.

Middelhoff, M., Cuisinier, O., Masrouri, F., Talandier, J., Conil, N., 2020. Combined impact of selected material properties and environmental conditions on the swelling pressure of compacted claystone/bentonite mixtures. Applied Clay Science 184, 105389.

Niandou, H., Shao, J., Henry, J., Fourmaintraux, D., 1997. Laboratory investigation of the mechanical behaviour of tournemire shale. International Journal of Rock Mechanics and Mining Sciences 34 (1), 3–16.

Orucoglu, E., Tournassat, C., Robinet, J. C., Made, B., Lundy, M., 2018. From experimental variability to the sorption related retention parameters necessary for performance assessment models for nuclear waste disposal systems: The example of pb adsorption on clay minerals. Applied Clay Science 163, 20–32.

Otani, J., Mukunoki, T., Obara, Y., 2000. Application of x-ray ct method for characterization of failure in soils. Soils and Foundations 40 (2), 111–118.

Pardoen, B., Bésuelle, P., Dal Pont, S., Cosenza, P., Desrues, J., 2020. Accounting for small-scale heterogeneity and variability of clay rock in homogenised numerical micromechanical response and microcracking. Rock Mechanics and Rock Engineering in press, 1–20.

Robinet, J.-C., 2008. Minéralogie, porosité et diffusion des solutés dans l'argilite du callovo-oxfordien de bure (meuse, haute-marne, france) de l'échelle centimétrique à micrométrique. Ph.D. thesis, Poitiers.

Robinet, J. C., Sardini, P., Coelho, D., Parneix, J. C., Pret, D., Sammartino, S., Boller, E., Altmann, S., 2012. Effects of mineral distribution at mesoscopic scale on solute diffusion in a clay-rich rock: Example of the callovo-oxfordian mudstone (bure, france). Water resources research 48, W05554.

Seghir, R., Witz, J. F., Courdert, S., 2014. Yadics-digital image correlation 2/3d software.

Shi, H., Hosdez, J., Rougelot, T., Xie, S., Shao, J., Talandier, J., 2020a. Analysis of local creep strain field and cracking process in claystone by x-ray micro-tomography and digital volume correlation. Submitted to Rock Mechanics and

Rock Engineering.

Shi, H., Hosdez, J., Rougelot, T., Xie, S., Shao, J., Talandier, J., Lacidogna, G., 2020b. Digital volume correlation applied to x-ray micro-tomography images in uniaxial creep tests on anisotropic clayey rock. Applied Sciences 10 (14), 4898.

Stavropoulou, E., Ando, E., Roubin, E., Lenoir, N., Tengattini, A., Briffaut, M., Besuelle, P., 2020. Dynamics of water absorption in callovo-oxfordian claystone revealed with multimodal x-ray and neutron tomography. Front. Earth Sci. 8:6, 10.3389/feart.2020.00006.

Stock, S. R., 2008. Recent advances in x-ray microtomography applied to materials. International Materials Reviews 53 (3), 129–181.

Togashi, Y., Kikumoto, M., Tani, K., 2017. An experimental method to determine the elastic properties of transversely isotropic rocks by a single triaxial test. Rock Mechanics and Rock Engineering 50 (1), 1–15.

Ulm, F. J., Abousleiman, Y., 2006. The nanogranular nature of shale. Acta Geotechnica 1, 77–88.

Viggiani, G., Besuelle, P., Desrues, J., 2013. X-ray micro tomography as a tool for studying localized damage/deformation in clay rock. Tech. Rep. 1.

Viggiani, G., Lenoir, N., Bésuelle, P., Michiel, M., Marello, S., Desrues, J., Kretzschmer, M., 2004. X-ray microtomography for studying localized deformation in fine-grained geomaterials under triaxial compression. Comptes rendus Mécanique 332 (10), 819–826.

Wang, L. L., Bornert, M., Heripre, E., Chanchole, S., Pouya, A., Halphen, B., 2015. The mechanisms of deformation and damage of mudstones: a micro-scale study combining esem and dic. Rock Mechanics and Rock Engineering 48, 1913–1926.

Wang, L. L., Yang, R. W., Chanchole, S., Zhang, G. Q., 2017. The time-dependent swelling of argillaceous rock under resaturated conditions. Applied Clay Science 146, 186–194.

Yang, D. S., Chanchole, S., Valli, P., Chen, L. F., 2013. Study of the anisotropic properties of argillite under moisture and mechanical loads. Rock Mechanics and Rock Engineering 46, 247–257.

Yang, S.-Q., Ju, Y., Gao, F., Gui, Y.-L., 2016. Strength, deformability and x-ray micro-ct observations of deeply buried marble under different confining pressures. Rock Mechanics and Rock Engineering 49 (11), 4227–4244.

414 Zeng, Z., J, C. Y., Zhang, F., Talandier, J., Conil, N., 2019. Investigation of swelling pressure of bentonite/claystone
415 mixture in the full range of bentonite fraction. Applied Clay Science 178, 105137.
416 Zhang, C., Armand, G., Conil, N., Laurich, B., 2019. Investigation on anisotropy of mechanical properties of callovo-
417 oxfordian claystone. Engineering geology 251, 128–145.
418 Zhang, F., Xie, S. Y., Hu, D. W., Shao, J. F., Gatmiri, B., 2012. Effect of water content and structural anisotropy on
419 mechanical property of claystone. Applied Clay Science 69, 79–86.